







New targets for drug design: importance of nsp14/nsp10 complex formation for the 3'-5' exoribonucleolytic activity on SARS-CoV-2

Margarida Saramago , Cátia Bárria , Vanessa G. Costa , Caio S. Souza , Sandra C. Viegas , Susana Domingues , Diana Lousa , Cláudio M. Soares , Cecília M. Arraiano  and Rute G. Matos 

Instituto de Tecnologia Química e Biológica António Xavier, Universidade Nova de Lisboa, Oeiras, Portugal

Keywords

coronavirus; *in vitro* activity; molecular modeling; MTase; nsp10; nsp14; RNase; SARS-CoV-2

Correspondence

M. Saramago, C. M. Arraiano and R. G. Matos, ITQB NOVA, Av. da República, 2780-157 Oeiras, Portugal.
E-mails: margaridasaramago@itqb.unl.pt, cecilia@itqb.unl.pt, rmatos@itqb.unl.pt

Margarida Saramago, Cátia Bárria and Vanessa G. Costa should be regarded as joint first authors

(Received 8 January 2021, revised 16 February 2021, accepted 8 March 2021)

doi:10.1111/febs.15815

SARS-CoV-2 virus has triggered a global pandemic with devastating consequences. The understanding of fundamental aspects of this virus is of extreme importance. In this work, we studied the viral ribonuclease nsp14, one of the most interferon antagonists from SARS-CoV-2. Nsp14 is a multifunctional protein with two distinct activities, an N-terminal 3'-to-5' exoribonuclease (ExoN) and a C-terminal N7-methyltransferase (N7-MTase), both critical for coronaviruses life cycle, indicating nsp14 as a prominent target for the development of antiviral drugs. In coronaviruses, nsp14 ExoN activity is stimulated through the interaction with the nsp10 protein. We have performed a biochemical characterization of nsp14-nsp10 complex from SARS-CoV-2. We confirm the 3'-5' exoribonuclease and MTase activities of nsp14 and the critical role of nsp10 in upregulating the nsp14 ExoN activity. Furthermore, we demonstrate that SARS-CoV-2 nsp14 N7-MTase activity is functionally independent of the ExoN activity and nsp10. A model from SARS-CoV-2 nsp14-nsp10 complex allowed mapping key nsp10 residues involved in this interaction. Our results show that a stable interaction between nsp10 and nsp14 is required for the nsp14-mediated ExoN activity of SARS-CoV-2. We studied the role of conserved DEDD catalytic residues of SARS-CoV-2 nsp14 ExoN. Our results show that motif I of ExoN domain is essential for the nsp14 function, contrasting to the functionality of these residues in other coronaviruses, which can have important implications regarding the specific pathogenesis of SARS-CoV-2. This work unraveled a basis for discovering inhibitors targeting specific amino acids in order to disrupt the assembly of this complex and interfere with coronaviruses replication.

Abbreviations

2'-O-MTase, 2'-O-methyltransferase; CoVs, coronaviruses; EDC, 3-dimethylaminopropyl-3-ethylcarbodiimide; ExoN, N-terminal 3'-to-5' exoribonuclease; HCoV, human coronavirus; IFN-I, type I interferon; IMAC, immobilized metal affinity chromatography; m⁷G, N7-methylguanosine; MERS, Middle East respiratory syndrome; MHV, mouse hepatitis virus; N7-MTase, C-terminal N7-methyltransferase; NHS, N-hydroxysuccinimide; nsp, nonstructural protein; PDB, protein data bank; RMSD, root-mean-square deviation; RNase, ribonuclease; RU, response units; SAM, S-adenosyl methionine; SARS, severe acute respiratory syndrome; SPR, surface plasmon resonance; TLC, thin layer chromatography.

Introduction

Over the last years, we have observed the emergence of different coronaviruses (CoVs) that have caused serious human epidemic diseases such as the severe acute respiratory syndrome (SARS) in 2002, the Middle East respiratory syndrome (MERS) in 2012, and, currently, the pandemic coronavirus disease-2019 (COVID-19).

SARS-CoV-2 is the causative agent of COVID-19 and belongs, together with SARS-CoV and MERS-CoV, to the genera *Betacoronavirus*. All these three viruses emerged as novel coronaviruses, considered to have initially been transmitted to humans from animals (zoonotic viruses), and all cause respiratory illnesses [1].

CoVs are enveloped, single-stranded positive-sense RNA viruses from the order *Nidovirales* that have the largest genome among RNA viruses (~30 kb in the case of SARS-CoV-2) [2]. SARS-CoV-2 contains a large replicase gene that occupies two-thirds of the genome encompassing nonstructural proteins (nsps), followed by structural and accessory genes. Among the nsp proteins, there is the nsp14 ribonuclease.

Ribonucleases (RNases) are key factors in the control of all biological processes. These enzymes ensure maturation, degradation, and quality control of all types of RNAs in all domains of life [3–7]. Nsp14 protein has exoribonucleolytic activity conferred by its N-terminal ExoN domain [8]. The ExoN domain resembles the superfamily of DEDDh exonucleases, which also include the proofreading domains of many DNA polymerases as well as other eukaryotic and prokaryotic exonucleases [9]. These enzymes catalyze the excision of nucleoside monophosphates from nucleic acids in the 3'-to-5' direction, using a mechanism that depends on two divalent metal ions and a reactive water molecule [10–12]. This exonucleolytic activity is critical for the proofreading activity during coronavirus replication, a property missing in other RNA viruses, which enhances its replication fidelity and has played an important role in nidoviral evolution and genome expansion [13].

SARS-CoV-2 and SARS-CoV share 79.5% of genome homology, and much of what is presently known about the biology of SARS-CoV-2 was inferred from previous studies on SARS-CoV [14]. However, some striking differences suggest important differences between the two CoVs in terms of infectiousness and the effects they have on human hosts.

Despite the high amino acid sequence identity (95%) between the nsp14 of both viruses, SARS-CoV ExoN knockout mutants are viable, even with an increased mutation frequency, while the equivalent ExoN knockout mutants of SARS-CoV-2 are nonviable [15]. This striking difference suggests an additional and critical

ExoN function in SARS-CoV-2 replication. Nsp14 ExoN seems to have a very important role in SARS-CoV-2 RNA synthesis [15], showing up as a prominent target for the development of antiviral drugs.

Whereas basal nsp14 ExoN activity does not require the presence of cofactors, its activity is only fully activated in the presence of the nsp10 protein [16]. The crystal structure of SARS-CoV nsp14 in complex with its nsp10 cofactor has shed light on how the interaction between the proteins occurs [17].

The N7-methylguanosine (m⁷G) cap is a defining structural feature of eukaryotic mRNAs, including those of eukaryotic viruses that replicate in the cytoplasm. SARS-CoV nsp14 was discovered to be a bifunctional protein, since beyond its exoribonucleolytic activity it also displays a guanine-N7-methyltransferase (N7-MTase) activity in its C-terminal domain [18]. This means that the enzyme is capable of methylating cap analogues or GTP substrates, in the presence of S-adenosyl methionine (SAM) as methyl donor [18,19]. The nsp14 N7-MTase activity is essential for the formation of a functional 5' RNA cap structure, critical for stability, and translation of CoV mRNAs in the host cells. In fact, mRNA cap methylation requires the concerted action of three viral proteins: nsp14, nsp10, and nsp16. Additionally to nsp14, nsp10 is also responsible for stimulating the activity of nsp16 2'-O-MTase, which makes this protein a central player in RNA cap methylation [20]. The obligate sequence of methylation events is initiated by nsp14, which first methylates capped RNA transcripts to generate cap-0 ⁷MeGpppA-RNAs. The latter are then selectively 2'-O-methylated by the 2'-O-MTase nsp16 in complex with its activator nsp10 to give rise to cap-1 ⁷MeGpppA_{2'-OMe}-RNAs. While nsp14 recognizes non-methylated RNA cap exclusively, nsp10/nsp16 recognizes N7-methylated RNA cap [20].

Coronaviruses have the inherent capacity to mutate, recombine, and infect different hosts. This raises an urgent need for the development of effective antiviral drugs to fight against the present and future pandemic diseases that may arise. Through its dual function, nsp14 protein plays a prominent role in CoV life cycle, and, thus, it is a very attractive target for drug design. Its N7-MTase activity is involved in RNA cap modification to assist in translation and evading host defenses, while the 3'-5' ExoN activity (stimulated by nsp10) has a direct role in CoV RNA synthesis beyond assuring the long-term genome fidelity.

In this work, we provide a biochemical characterization of SARS-CoV-2 nsp14/nsp10, addressing several aspects of this complex for the first time. By contributing to the deep understanding of nsp14/nsp10

mechanisms of action, this work will also help to clarify its role in the SARS-CoV-2 life cycle. Importantly, it will serve as a basis for the design of effective drugs to treat COVID-19 and other CoV infections.

Results

ExoN activity of nsp14 is stimulated in the presence of nsp10

We have purified both SARS-CoV-2 nsp10 and nsp14 proteins individually through immobilized metal affinity chromatography (IMAC) followed by size-exclusion chromatography based on previous works [16,21] (Materials and Methods section). As shown in Fig. 1A, nsp10 and nsp14 migrate at 17 kDa and 62 kDa, respectively, consistent with their expected molecular weights. In the case of nsp10, which is known to have 12 identical subunits assembled into a spherical dodecameric architecture [22], the visible higher bands (highlighted with an asterisk *) correspond to reminiscent oligomers of the protein. This was further confirmed by western blot using antibodies specific for the His-tag tail of the protein (data not shown).

First, we intended to test the ribonuclease activity of the purified SARS-CoV-2 nsp14. We have used the synthetic RNA substrate H4 previously reported in Bouvet *et al.* [16]. This substrate is a 22-nucleotide (nt) long RNA with a 5' single-stranded (ss) tail and a 3'-end engaged in a stable duplex structure (Fig. 1B). The nsp14 ExoN activity was then determined by analyzing the hydrolysis of the H4 RNA 5'-end radiolabeled. As we can see in the left panel of Fig. 1C, nsp14 alone exhibits exoribonucleolytic activity; however, in the conditions tested (40 nM of nsp14), the activity was not pronounced. (Fig. 1C). Nsp10 was previously reported as a critical cofactor for the activation of nsp14 ExoN activity in SARS-CoV [16,17]. As such, we have analyzed the influence of nsp10 in the activity of SARS-CoV-2 nsp14, using different molar ratios between nsp14 and nsp10 (Fig. 1C). SARS-CoV-2 nsp14 ExoN activity was found to be stimulated by nsp10 in a dose-dependent manner. At equimolar ratio (1:1), the ExoN activity is weakly stimulated compared with the ExoN activity exhibited by nsp14 alone. By increasing the concentration of nsp10, the maximal ExoN activity was achieved with a ratio nsp14-nsp10 of 1:4, in agreement with the results reported for SARS-CoV and MERS-CoV [15,16]. In this condition, we observe a faster RNA degradation and almost complete disappearance of the full-length RNA after 30 minutes of incubation. The degradation products formed range between 17- and 20-nts in length, which

corresponds to cleavage from the 3'-end of the RNA duplex region of the 22-nt long H4 RNA. By increasing the concentration of nsp14 (and also of nsp10 proportionally), the hydrolysis of the substrate becomes much more efficient, yielding smaller breakdown products corresponding to degradation of the ss- and double-stranded (ds) regions (Fig. 1C, right panel). The ladder-like pattern of the degradation products is typical of exoribonucleolytic cleavage of the RNA in the 3'-5' direction (considering that the RNA is labeled at the 5' end), further supporting CoVs nsp14 3'-5' directionality [15,16,23]. As a control, we have tested nsp10 alone (at 160 nM, which was the higher concentration used in nsp10:nsp14 ratio) for ribonucleolytic activity under the same conditions used for nsp14. As expected, nsp10 was not able to degrade the RNA substrate (Fig. 1C).

The ability of nsp10 to interact with nsp14 was analyzed through surface plasmon resonance (SPR) (Fig. 1D). For this, purified nsp14 was immobilized in a sensor chip and nsp10 was injected at different concentrations as described in Materials and Methods. The results confirm that both proteins interact with each other as showed by an increased response when nsp10 is injected. This increase is dependent on nsp10 concentrations, as confirmed by the titration graph (Fig. 1D, right panel), and it is possible to see the dissociation of nsp10 over time when injection stops (Fig. 1D, left panel). Since nsp14 or nsp10 were shown to be very unstable proteins, it was not possible to obtain a good fit of the data in order to determine the binding kinetics and dissociation constants.

We have also copurified nsp10 and nsp14 proteins. The chromatograms referring to the purification of nsp10 and nsp14 alone and nsp10:nsp14 copurified are represented in Fig. 1E, on the left. It is possible to see that, when copurified, there are some peaks between 7 and 12 mL that do not appear when the proteins are purified alone. Moreover, the peaks corresponding to nsp14 and nsp10 alone are shifted to the left when both proteins are copurified. Several fractions corresponding to the different peaks during the copurification were collected and SDS/PAGE analysis shows the presence of both nsp14 and nsp10 proteins in all fractions and in different ratios (Fig. 1E), confirming their interaction. We then tested the ExoN activity of some of the eluted fractions (Fig. 1E, gel, on the right). Fraction 16 that appears to have an equimolar proportion of nsp14-nsp10 exhibited increased activity and degraded the full-length RNA in 15 minutes, with major breakdown products of 18-, 17-, and 16-nts. 25 nM of this fraction was sufficient to degrade all the full-length substrate, whereas for the mixture of nsp14 and nsp10 separately purified, 40 nM and 160 nM have

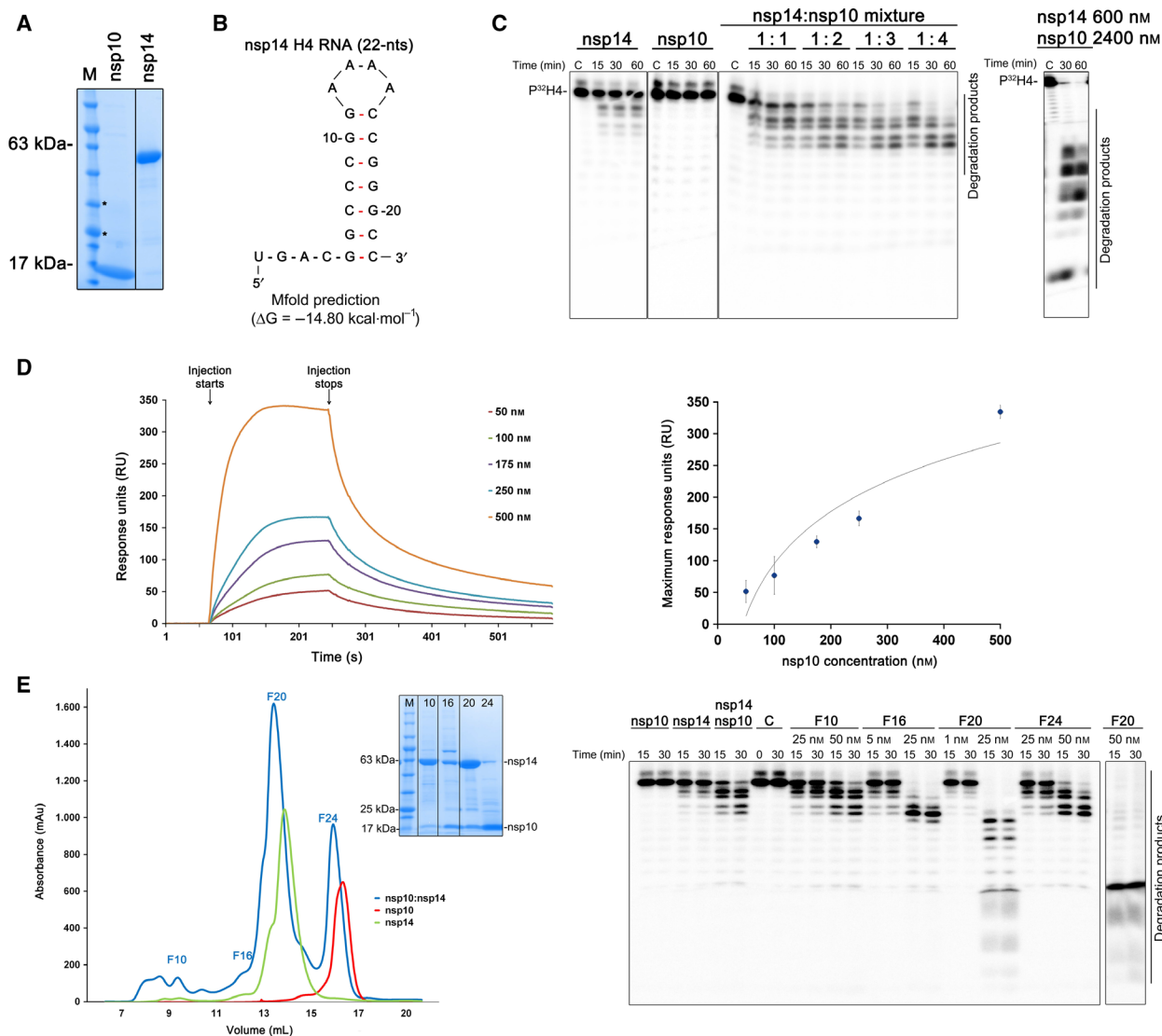


Fig. 1. ExoN activity of nsp10:nsp14 complex. (A) SDS/PAGE analysis of the purified nsp14 and nsp10 WT proteins. Samples were denatured and separated in a Novex™ 8-16% Tris/Glycine Gel (Invitrogen™). Gel was stained with BlueSafe (NZYTech, Portugal) to visualize protein bands. NZYColour Protein Marker II (NZYTech, Portugal) was used as a molecular weight marker, and its respective band sizes are represented in both gels. (B) Predicted secondary structure adopted by H4 RNA substrate used in the RNase assays. Its most stable structure (minimum free energy (ΔG) of $-14.80 \text{ kcal}\cdot\text{mol}^{-1}$) was predicted using Mfold RNA modeling server (http://www.unafold.org/RNA_fold.html). (C) Activity of nsp14 and nsp10 alone or in combination using 50 nM of H4 RNA substrate. In the left panel, nsp14 was used at 40 nM; nsp10 was used at 40 nM in 1 : 1 ratio, 80 nM in 1 : 2 ratio, 120 nM in 1 : 3 ratio, and 160 nM in 1 : 4 ratio. In the right panel, nsp14 was tested at 600 nM in the presence of nsp10 at 2400 nM (1 : 4 ratio). Reactions were run on 7 M urea/20% polyacrylamide gel. C, control reactions; time points are indicated in the top of each panel. (D) Surface plasmon resonance analysis. Sensorgram (left) and titration (right) curves corresponding to the interaction between nsp14 and nsp10 proteins. Nsp10 was injected over nsp14 at the concentrations indicated in the figure. The sensorgram represents the average of three independent injections of each concentration. (E) Copurification of nsp14 and nsp10. The chromatograms corresponding to the purification of nsp10 and nsp14 alone and nsp10:nsp14 copurified are represented on the left. On the top right, it is represented a 15% SDS/PAGE with the fractions collected during the SEC. In the right panel, the activity of some fractions (F10, F16, F20, and F24) was analyzed using 50 nM of H4 RNA substrate. Protein concentration used is indicated in the figure. Reactions were analyzed on 7 M urea/20% polyacrylamide gels. C, control reactions; time points are indicated in the top of each panel. All the experiments were performed at least in triplicate.

been used, respectively (1 : 4 ratio). Surprisingly, fraction 20, which appears to have more nsp14 compared to nsp10, was the most active sample. This fraction showed the ability of totally consuming the RNA, starting with the ds-region and then proceeding to the ss-region of the substrate, generating products of smaller size. With 50 nM of this fraction, the degradation proceeds until it reaches a unique and final product of 8-nts (Fig. 1E). This result is in line with the reported ability of SARS-CoV nsp14 to hydrolyze ssRNA to end products of 8–12 nts [16,23]. Finally, fractions 10 (excess of nsp14) and 24 (excess of nsp10) present a similar ability to cleave the H4 RNA. The activity of these fractions was comparable to that observed when testing nsp14 and nsp10 mixed together in the 1:4 ratio (Fig. 1E). We can conclude that copurifying nsp14 and nsp10 proteins substantially increases nsp14 ExoN activity, and, in this case, the ratio between them seems not to be determinant to achieve high levels of ExoN activity. However, taking into account that our intention was the study of several mutant versions of these proteins from SARS-CoV-2, and considering the results obtained, the remaining experiments were performed with nsp14 and nsp10 purified separately. The fact that both nsp14 and nsp10 need a ratio in which nsp10 is in excess (Fig. 1C) may be an indication of the instability of the complex; otherwise, it might have maximum activity with a 1 : 1 ratio. Indeed, during the experimental part of this work, we noticed that the ExoN activity decreased with time and the activity is completely lost after two weeks. The same behavior was previously observed [24]. As such, all the experiments were performed with proteins freshly purified.

SARS-CoV-2 nsp14 ExoN activity is metal-dependent

The activity of the nsp14 ExoN domain is also known to be dependent on divalent cations [16,17,23,25]. In order to determine which divalent metals support maximal activity of the SARS-CoV-2 nsp14-nsp10 complex, we tested ExoN activity in the presence of different divalent ions: Mg²⁺, Mn²⁺, Ca²⁺, Ni²⁺, Cu²⁺, Co²⁺, or Zn²⁺ (Fig. 2). As already reported for several other RNases, binding of these different metal ions might affect the activity of SARS-CoV-2 ExoN by inducing structural changes in the active site [25–27]. The results show that SARS-CoV-2 ExoN nsp14 is active in the presence of both Mg²⁺ and Mn²⁺, with a more pronounced activity in the presence of Mg²⁺. When Mn²⁺ is added to the reaction, the activity is more distributive and smaller breakdown products with ladder-like pattern are visible (Fig. 2). Ca²⁺ did not support the

activity, in agreement with data obtained for SARS-CoV nsp14 and other proteins from the DEDD family [11,28]. The same was observed for Ni²⁺ and Cu²⁺ ions (Fig. 2). Interestingly, in the presence of Co²⁺ and Zn²⁺ we observed a residual, but not relevant ExoN activity (Fig. 2). Chen *et al.* [25] also reported nsp14 residual activity in the presence of Zn²⁺. Finally, the addition of the chelating agent EDTA to the reaction completely blocks nsp14 ExoN activity (Fig. 2), confirming the importance of divalent ions, namely Mg²⁺ and Mn²⁺, for this activity, similar to that described for the SARS-CoV counterpart [16,24,25]. One question that may be raised is as follows: Are the divalent ions affecting the complex formation or are they simply affecting nsp14 active site? To address this question, we have performed the same experiment with nsp14 alone but using higher protein concentrations (1 μM) so that we could visualize RNA cleavage in the absence of nsp10. The results obtained are similar to the ones presented in Fig. 2 (data not shown) meaning that the divalent ions are affecting nsp14 active site and not the complex formation.

SARS-CoV-2 nsp10 residues involved in nsp14-10 complex formation showed that the stability of this complex is determinant for ExoN activity

Until now, there is no available structure for the SARS-CoV-2 nsp14-nsp10 complex. As such, we have modeled the SARS-CoV-2 nsp14-nsp10 complex based on the 3D structure of the complex from SARS-CoV (PDB ID 5C8S) (Fig. 3A,B) [17]. This was possible due to the sequence and structural similarities between nsp10 and nsp14 proteins between the two viruses (Figs 4A and 5A). The crystal structure of the isolated nsp10 from SARS-CoV-2 was recently solved, and all-atom RMSD between this structure and the one from the SARS-CoV nsp10-nsp14 complex is 1.36 Å [29]. However, the isolated nsp10 structure from SARS-CoV-2 was not used in the modeling, since we wanted to keep the nsp14-nsp10 native contacts as much as possible. The all-atom RMSD between the generated model (Fig. 3) and the crystal structure of SARS-CoV nsp10-nsp14 complex was 0.76 Å. Comparing with the SARS-CoV-2 nsp10 structure, our model showed an all-atom RMSD of 1.33 Å, which is in agreement with the deviations found between the crystal structures. The model is represented in Fig. 3B, and as we can see the interaction between nsp14 and nsp10 is figuratively similar to a ‘hand (nsp14) over fist (nsp10)’.

Conserved amino acids located on the surface of nsp10 were reported to be involved in nsp14-nsp10 interaction in other CoVs [16,21,30,31]. As such, and

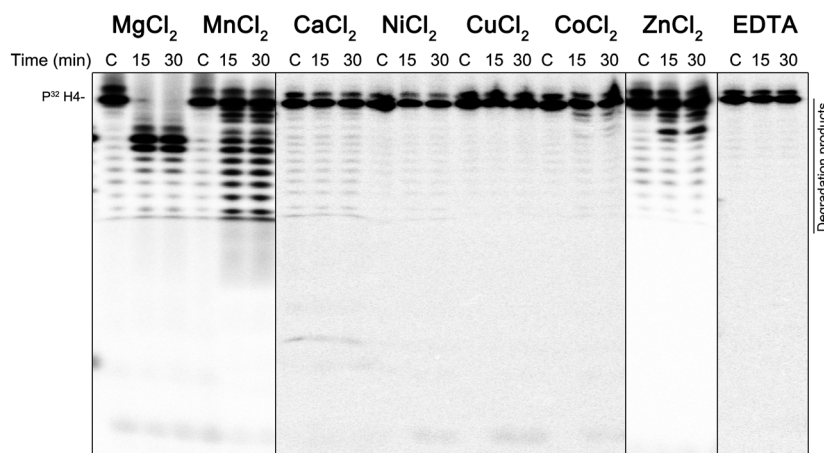


Fig. 2. Metal cofactor-dependent activity of nsp14. nsp14:nsp10 complex (40 nM:160 nM) was incubated with 5 mM of different divalent ions. Reactions were analyzed on 7 M urea/20% polyacrylamide gels. C, control reactions; time points are indicated in the top of each panel. All the experiments were performed at least in triplicate.

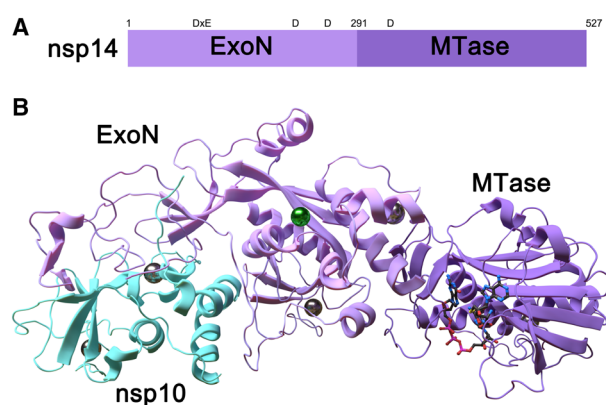


Fig. 3. (A) Scheme of nsp14 domain organization. ExoN domain, aa 1-291; MTase domain, aa 292-527. (B) Homology model of the nsp10-nsp14 complex of SARS-CoV-2. The nsp10 is marked in cyan. The MTase and ExoN domains of nsp14 are marked in dark and light purple, respectively. The complex was refined in the presence of Mg²⁺ (green sphere) and Zn²⁺ (gray spheres) ions, and the substrates SAH and GpppA (sticks).

in order to study their role in ExoN activity, we mutated some of these amino acids (highlighted in red boxes in Fig. 4A) into alanines creating the point mutants F19A, G69A, S72A, H80A, and Y96A. As shown in the sequence alignment of the SARS-CoV-2 nsp10 protein with the nsp10 from the two other highly pathogenic and deadly human coronaviruses SARS-CoV and MERS (Fig. 4A), these amino acids are conserved among the three CoVs with the exception of Y96. This residue is unique to SARS-CoV and SARS-CoV-2, whereas a phenylalanine (F96) is found in most other CoVs, including MERS that belongs to a different lineage of the *betacoronavirus* genus [31].

Indeed, the sequence alignment (Fig. 4A) reveals that the three proteins present a high degree of sequence conservation, with SARS-CoV-2 nsp10 being more closely related to SARS-CoV (97.1% of sequence identity and 99.3% of sequence similarity).

Substitution of these residues by an alanine is not expected to drastically alter the structures of these nsp10 protein variants comparing to that of the nsp10 wild-type (WT), as confirmed by NMR for SARS-CoV nsp10 mutants [30,31,32]. His-tagged nsp10 mutant derivatives were expressed in *E. coli* and purified (Fig. 4B). The functional consequences of these nsp10 mutations were evaluated in terms of their interaction with nsp14 through SPR. As expected the instability of these proteins, only enabled us to access the interaction of 75 nM of each version with immobilized nsp14, without determining the kinetics of the reaction. As we can see in Fig. 4C, F19A and S72A have their ability to interact with nsp14 reduced, whereas G69A, H80A, and Y96A have apparently completely lost their ability to interact with nsp14 WT in these conditions.

According to our homology model represented in Fig. 4E, the alanine substitutions affect the binding between nsp10 and nsp14 in different ways. The F19A mutation seems to weaken the van der Waals interactions of nsp10 with the helix H4 of the nsp14 (Fig. 4E). This can represent the loss of an important hydrophobic effect at the interface of the two proteins. On one end, this helix is part of the framework that keeps key catalytic residues and an Mg²⁺ ion in place in the ExoN active site, whereas the other end is extended by a loop that forms a zinc finger that is crucial for the structural stability of the nsp14 from SARS-CoV [17]. The binding of nsp10 to this region avoids the exposure of hydrophobic amino acids to the solvent and helps the stabilization of the protein structure.

A

SARS-CoV-2	1	AGNATEV PANSTVL SFCFA F AVDAAKAYKDYLASGGQPI TNCVKMLCTHTGTGQAI TVTPE
SARS-CoV	1	AGNATEV PANSTVL SFCFA F AVDPAKAYKDYLASGGQPI TNCVKMLCTHTGTGQAI TVTPE
MERS	1	AGSNT EFA S NS SVLSL VNF T VDPQKAYLDFVNAGGAPLITNCVKMLTPKGTGTGI AI SVKPE

SARS-CoV-2	61	ANMDQESFGGAS C CLYCRCHI DHPNPKGFCDLKGGYVQI PTTCANDPVGFTLKNTVCTVC
SARS-CoV	61	ANMDQESFGGAS C CLYCRCHI DHPNPKGFCDLKGGYVQI PTTCANDPVGFTLRNTVCTVC
MERS	61	STADQETYGGA S VCLYCR A HI EHPDVS G VCKYKGGK F VQI PAQCVRDPVGFCLSNTPCNVC

SARS-CoV-2	121	GMWKGYGCS CDQL REPML- Q
SARS-CoV	121	GMWKGYGCS CDQL REPL M- Q
MERS	121	QYWI G YGCNCDSL RQAALPQ

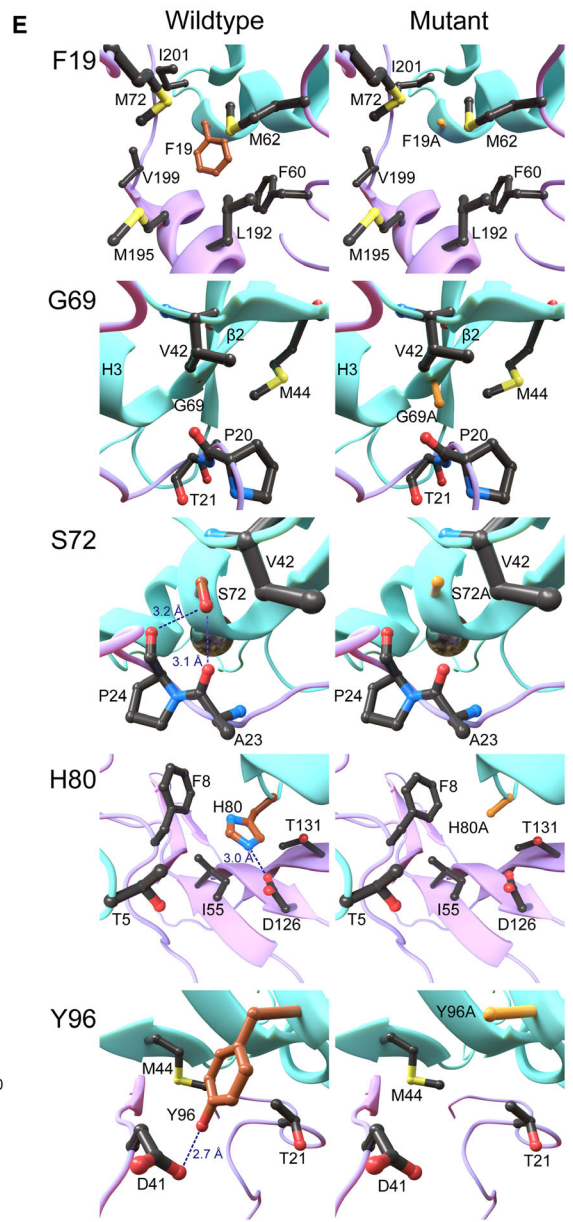
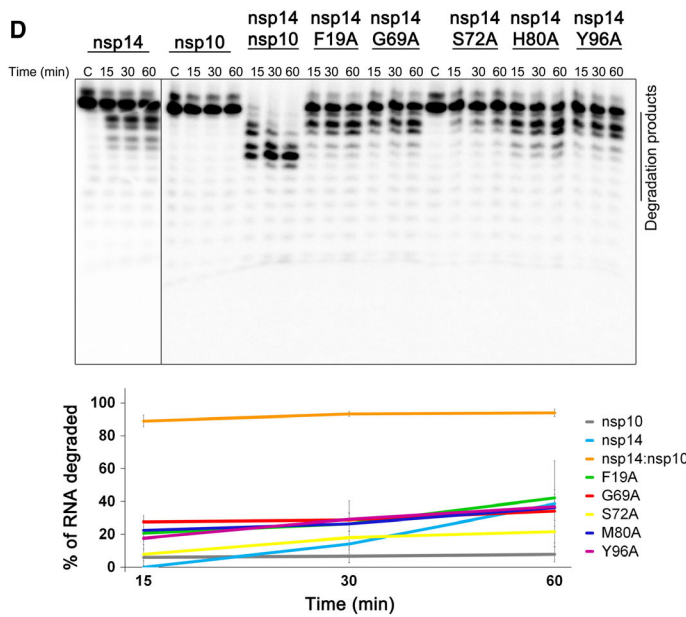
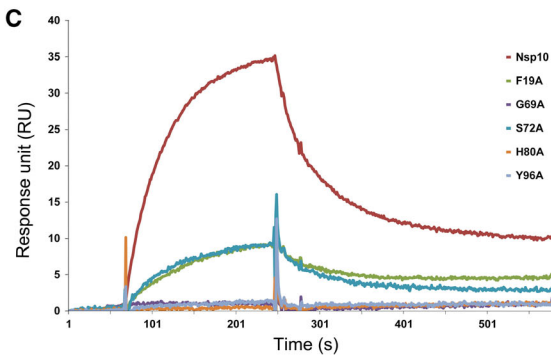
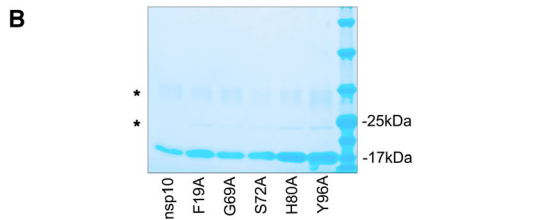


Fig. 4. Influence of nsp10 mutations on nsp14-nsp10 complex formation and ExoN activity. (A) Sequence alignment of nsp10 from SARS-CoV-2 (UniProt ID: [P0DTD1](#)), SARS-CoV (UniProt ID: [P0C6X7](#)), and MERS (YP_009047225). Residues mutated in this work are highlighted with a red box. (B) SDS/PAGE analysis of the purified nsp10 WT and mutant versions F19A, G69A, S72A, H80A, Y96A. Samples were denatured and separated in a Novex™ 8-16% Tris/Glycine Gel (Invitrogen™). Gel was stained with BlueSafe (NZYTech, Portugal) to visualize protein bands. NZYColour Protein Marker II (NZYTech, Portugal) was used as a molecular weight marker, and its respective band sizes are represented. (C) Surface plasmon resonance analysis. Nsp10 WT and mutant versions were injected over nsp14 at a concentration of 75 nM. The sensorgram represents the average of three independent injections of each protein. (D) Activity of nsp14 (40 nM) in the presence of nsp10 WT and mutant versions (160 nM). Reactions were analyzed on 7 M urea/20% polyacrylamide gels. C, control reactions; time points are indicated in the top of each panel. All the experiments were performed at least in triplicate. The % of H4 RNA degraded by nsp14 WT and nsp10 mutant versions was determined and represented in the bottom panel. (E) Position of the nsp10 mutations and their neighboring residues. The WT and mutated structures of F19A, G69A, S72A, H80A, and Y96A mutations are depicted on the left and right columns, respectively. Carbons of the WT and mutated residues are colored in brown and orange, respectively. Hydrogen bond and salt-bridges are marked in dashed lines with the respective distances. The nsp10 and nsp14 secondary structures are marked in cyan and purple, respectively.

The residue G69 is located in a known structural motif that links the nsp10 sheet $\beta 2$ to the helix H3 (Fig. 4E). This motif is part of an extensive region of intermolecular interactions between nsp10 and nsp14 that also helps on the stabilization of the ExoN domain [16]. The presence of a glycine amino acid in this position also allows for the accommodation of the carbonyl group of nsp14 P20. In this scenario, the mutation G69A is likely to cause local changes to the nsp10 secondary structure and to create unfavorable interactions with P20 and, thus, may interfere on the fitting between nsp10 and nsp14. This same region contains the residues S72, H80, and Y96, which participate in the network of polar interactions that connects nsp10 to nsp14. Specifically, residue H80 forms a salt-bridge with nsp14 D126 (Fig. 4E) while residue Y96 keeps a hydrogen bond with the carboxyl group of nsp14 D141 (Fig. 4E). Residue S72 is a special case as it makes hydrogen bonds with the carbonyl of nsp14 residues A23 and P24 (Fig. 4E). Thus, the substitution of these residues by alanine breaks intra- and intermolecular interactions that may be important not only for the binding between nsp10 and nsp14 but also to maintain their secondary structure.

Taken together, these mutations on nsp10 are prone to interfere on the interaction of this protein with nsp14. Evidence points to a stabilization role of nsp10 on the nsp14 structure and, thus, mutations that alter the binding between these proteins may disrupt the structure of the nsp14 ExoN domain and decrease its activity [16,17].

Since any alteration on the binding ability of nsp10 to nsp14 might modify the capacity of nsp14 ExoN to efficiently cleave RNA, we have also analyzed the effect of these nsp10 mutations on the activity of SARS-CoV-2 nsp14 ExoN. Time-course *in vitro* assays with 5'-end-labeled H4 RNA were performed in the presence of nsp10 WT or mutants (Fig. 4D), using the 1:4 nsp14-

nsp10 ratio as described above. All the nsp10 substitutions tested severely affected the nsp14 ExoN activity. Full disappearance of the RNA substrate was not detected even 60 min after incubation with any of the nsp10 variants, contrarily to that verified with the nsp10 WT, which allowed total degradation of the full-length RNA in 15 min. The major degradation products obtained from these reactions range between 19 and 20 nts, which correspond to cleavage in the ds-region of H4 RNA, observed for nsp14 alone, and no further progression is observed (Fig. 4D). Quantification of the amount of RNA degraded (Fig. 4D, bottom graph) showed that incubation with all nsp10 variants presents a similar result to nsp14 alone, while nsp14 in the presence of nsp10 WT degrades around 90% of the RNA in only 15 min. The most striking result was obtained with the S72A derivative that not only completely lost the ability to stimulate the exoribonucleolytic activity of nsp14, but also partially compromise the basal ExoN activity of nsp14 (Fig. 4D).

Overall, our results show that all nsp10 mutants have reduced nsp14 affinity when compared to the WT protein, with consequences for the stimulation effect on nsp14 ExoN activity (Fig. 4C,D). In agreement with this, the nsp10 F19A, G69A, S72A, H80A, and Y96A mutants were also shown to affect nsp14-nsp10 interaction in SARS-CoV and resulted in a low nsp14 ExoN activity, suggesting an important role for these residues in nsp14 recognition and interaction [21]. These results reinforce the idea that a stable interaction between nsp10 and nsp14 is strictly required for the nsp14-mediated ExoN activity of SARS-CoV-2.

ExoN motif I has a prominent role on the RNase activity of SARS-CoV-2 nsp14

SARS-CoV-2 nsp14 also has a high similarity with nsp14 from SARS-CoV (95% of sequence identity and

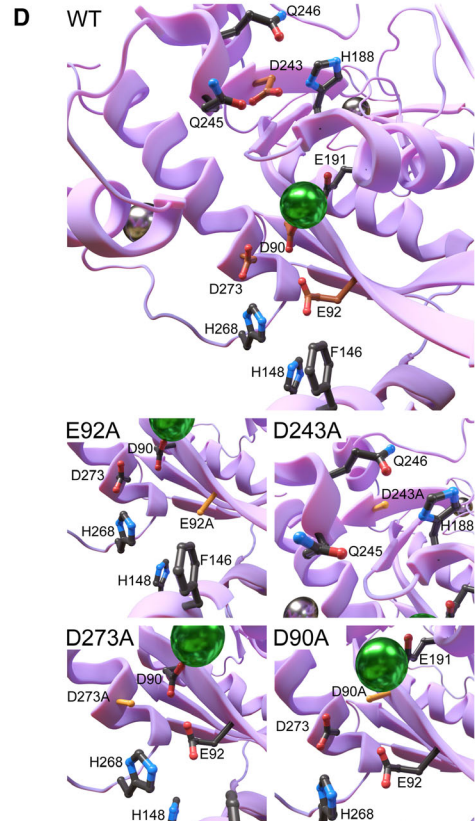
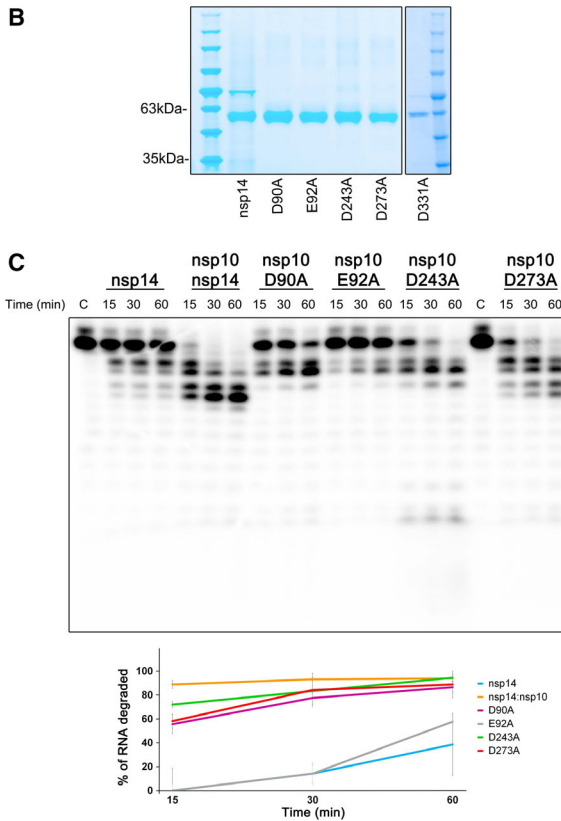
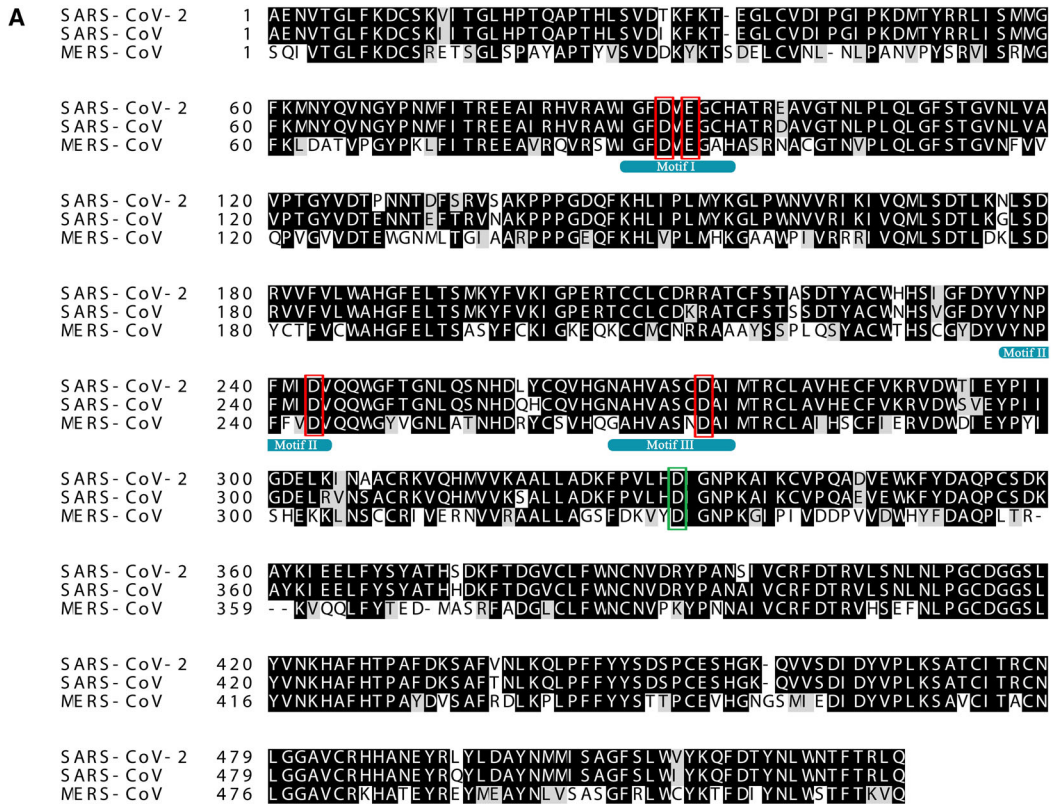


Fig. 5. Analysis of DEDD motif mutations for ExoN activity. (A) Sequence alignment of nsp14 from SARS-CoV-2 (UniProt ID: [P0DTD1](#)), SARS-CoV (UniProt ID: [P0C6X7](#)), and MERS (YP_009047225). Residues from the DEDD motif are highlighted with a red box and D331 in a green box. (B) SDS/PAGE analysis of the purified nsp14 WT and respective mutant versions D90A, E92A, D243A, D273A, and D331A. Samples were denatured and separated in a Novex™ 8-16% Tris/Glycine Gel (Invitrogen™). Gel was stained with BlueSafe (NZYTech, Portugal) to visualize protein bands. NZYColour Protein Marker II (NZYTech, Portugal) was used as a molecular weight marker, and its respective band sizes are represented. (C) Activity of nsp14 WT and mutant versions (40 nM) in the presence of nsp10 WT (160 nM). Reactions were analyzed on 7 M urea/20% polyacrylamide gels. C, control reactions; time points are indicated in the top of each panel. All the experiments were performed at least in triplicate. The % of H4 RNA degraded by nsp14 mutant versions and nsp10 WT was determined and represented in the bottom panel. (D) Structure of the modeled nsp14 ExoN domain and respective mutants. Overall structure of the WT ExoN domain with the side chain of residues subjected to alanine substitutions (carbon atoms marked in brown) and other residues that may participate in the exoribonuclease reaction. Magnesium and Zinc ions are depicted in green and gray spheres, respectively. The structure of the mutations E92A, D243A, D273A, and D90A is shown with carbons colored in orange. The side chains of nonmutated residues were kept fixed during the structure refinement

99.1% of sequence similarity), and less conservation with the amino acid sequence of MERS (Fig. 5A). As a bimodular protein, the amino acids 1–290 from SARS-CoV-2 nsp14 fold into the ExoN domain, and the amino acids 291–527 form the N7-MTase domain (Fig. 3A). In nsp14, the differences are spread punctually over the protein structure. However, none of these positions are inside the MTase or the ExoN active sites. The ExoN activity depends on the conserved DEEDh motif, which is part of the active site (Fig. 5A) [13,16,23]. These conserved active site residues were found to be distributed over three canonical motifs (I, II, and III). The SARS-CoV-2 residues D90/E92 (motif I), D243 (motif II), and D273 (motif III) are fully conserved in the three CoVs represented. Amino acid residues E92, D243, and D273 form an electrophilic environment that is important for substrate binding and catalysis on nsp14 of SARS-CoV-2 (Fig. 5D). Additionally, E92 is probably responsible for the coordination of the second Mg^{2+} ion necessary for the reaction. It may also form a hydrogen bond with H268, which is another key residue that anchors the substrates. We have constructed and purified nsp14 mutants with single substitutions of these conserved catalytic residues by the neutrally charged alanine (D90A, E92A, D243A, and D273A) (Fig. 5B). We conducted activity assays using these variants in order to assess the role of these amino acids in the ExoN activity of SARS-CoV-2 nsp14. The SARS-CoV and MERS nsp14 studies available so far reported that substitution of ExoN catalytic residues by alanine has a large impact in their exoribonucleolytic activity [15–17,23]. As shown in Fig. 5C, mutations on these residues influenced the ExoN activity of SARS-CoV-2 nsp14. E92A substitution had the most striking effect, presenting only residual exoribonuclease activity. Although to a less extent, the D90A mutant was also severely deficient in their ability to degrade RNA and

rendered a major product of 19 nts. These results demonstrate the importance of residues from motif I (D90 and E92) for the activity of nsp14. In contrast, mutations in aspartates from motifs II and III (D243A and D273A, respectively) led to a modest reduction in the ExoN activity, both being able to fully degrade the full-length RNA after 60 min of incubation (Fig. 5C). However, the cleavage patterns generated with both mutants were different. The nsp14 D273A version yielded products ranging between 17- and 20-nts (more similar to that of WT), whereas the D243A mutant generated major products between 18- and 20-nts. However, this mutant version was able to go further in the degradation since smaller minor products could be detected (Fig. 5C). This mutation may cause conformational changes in the active site of nsp14 ExoN, which allows the degradation of a fraction of the RNA substrate to smaller products. On the contrary, the substitutions D90A, E92A, and D273A in the nsp14 ExoN catalytic center may affect the binding to the 3' end of the RNA, which can make it difficult to bind to smaller products that are being produced at each cleavage event. This explains why these mutant versions render higher degradation products. Due to the extra role of the motif I E92 residue, it is likely that the substitution E92A causes a major impact on the catalysis compared with the mutations D243A and D273A. The residue D90 also coordinates an Mg^{2+} ion (Fig. 5D), but surprisingly the impact of the mutation D90A was not as severe as the observed on E92A. Probably, the presence of the residue E191 may be sufficient to keep the Mg^{2+} ion in the active site, attenuating the effects of the D90A substitution. This behavior is consistent with the data from SARS-CoV that shows that the E191 mutation is more likely to affect the ExoN activity than the mutation D90A [17].

In general, our observations contrast with the results obtained for SARS-CoV and recently for MERS [15–

17,23]. In the closely related SARS-CoV, the frequently used motif I-double substitution D90A/E92A resulted in a major reduction in ExoN activity, whereas the motif II D243A and motif III D273A mutations completely abrogated the ExoN activity [16,17,23]. Also in MERS, both D90A and E92A substitutions appeared to be slightly less detrimental than D273A, even though all of them resulted in almost complete loss of ExoN activity [15]. The results here reported revealed some differences on the functionality of the conserved catalytic residues D90, E92E, D243, and D273 from nsp14 ExoN, which can be related to the pathogenesis of SARS-CoV-2.

Nsp14 N7-MTase Activity is functionally independent of the ExoN activity

As already mentioned, nsp14 is a bifunctional enzyme with both ExoN and N7-MTase activities, connected by a hinge region that modulates the flexibility of the protein (Fig. 3A,B). The C-terminal MTase domain of nsp14 was found to be able to methylate cap analogues or GTP substrates, in the presence of SAM as methyl donor [18,33]. In this work, we have established an *in vitro* assay with purified SARS-CoV-2 nsp14 to test its N7-MTase activity, using capped 30-mer G*ppp-RNA as substrate (Fig. 6). An nsp14 D331A mutant was constructed and used as a negative

control due to its reported involvement in the binding of the methyl donor SAM in SARS-CoV [16,18,33]. The level of cap methyltransferase activity of nsp14 was evaluated by the conversion of G*ppp-RNA to m⁷G*ppp-RNA during the cap methyltransferase reaction in TLC analysis. Subsequent P1 digestion of the RNA substrates to individual nucleotides gives the ratio of m⁷G*pppG spot compared with G*pppG on the TLC plate phosphor image. SARS-CoV-2 nsp14 was able to methylate the G*pppG cap of RNAs since we can observe, in the corresponding lane, a main spot that comigrates with m⁷G*pppG marker (Fig. 6A). In contrast, treatment of G*ppp-RNA with nsp14 D331A mutant did not generate a similar product on the TLC plate (Fig. 6A). Instead, it gives a nucleotide product that comigrates with G*pppG marker resultant from the digestion of G*ppp-RNA with P1 nuclease.

To evaluate whether the nsp14 ExoN activity has any influence on the SARS-CoV-2 MTase activity, the point mutations located in the conserved motifs of the ExoN domain (D90A, E92A, D243A, and D273A) were also tested for their capacity to methylate the G*ppp-RNA in the presence of SAM. As shown in Fig. 6B, none of these substitutions influence nsp14 MTase activity, in line with [33].

It has been reported that nsp10 exclusively interacts with the ExoN domain of nsp14 without perturbing the N7-MTase activity [16,34]. In fact, our results

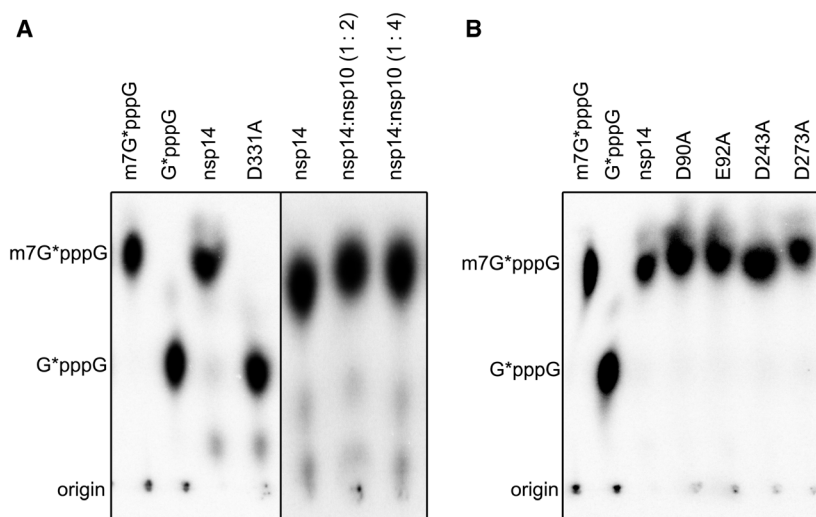


Fig. 6. Nsp14 MTase activity. (A) TLC analysis of nuclease P1-resistant cap structures released from the G*ppp-RNA methylated by nsp14 WT, D331A mutant, and nsp14 WT in the presence of nsp10 (1 : 2 and 1 : 4 ratios). (B) TLC analysis of nuclease P1-resistant cap structures released from the G*ppp-RNA methylated by nsp14 WT and nsp14 ExoN catalytic mutants D90A, E92A, D243A, and D273A. On the left of both images, we have the P1 digestions of the m⁷G*ppp-RNA and G*ppp-RNA produced by the commercially available vaccinia capping enzyme that was used as markers for m⁷G* and G*. The positions of origin and migration of m⁷G*pppG/G*pppG (lanes 1–2) are indicated on the right.

demonstrate that nsp14 presents a robust MTase activity in the absence of nsp10 (Fig. 6). To evaluate the influence of nsp10 in the MTase reaction, a smaller amount of nsp14 was assayed in the presence of nsp10 (1:2 and 1:4 ratios), so that we could observe some unmethylated G*pppG (Fig. 6A, right panel). As we can see, no differences on the MTase efficiency were found in the presence or absence of nsp10.

From this part of the work, we can conclude that the C-terminal region of SARS-CoV-2 nsp14 functions as an MTase and that this domain is functionally independent of the D90A, E92A, D243A, and D273A ExoN catalytic residues. The nsp14 MTase activity also seems to be independent on the presence of nsp10 cofactor, contrarily to nsp14 ExoN.

Discussion

The 16 nonstructural proteins (nsp1-16) encoded by the coronavirus genome (ORF1a/1b) are involved in viral replication and represent potential targets for antiviral drug discovery. Among these, nsp14 is a bifunctional enzyme that harbors both N-terminal ExoN and C-terminal N7-MTase activities [17,18,23]. The combination of both activities is unique for coronaviruses. Its ExoN activity is stimulated through the interaction with other nonstructural protein, nsp10, which constitutes a critical regulator of viral RNA synthesis and degradation. Due to the central role of the nsp14-nsp10 complex, we have performed a detailed characterization of these proteins from SARS-CoV-2, the coronavirus responsible for the current COVID-19 pandemic.

Nsp10 residues involved in the interaction with nsp14 were found to be essential for SARS-CoV and MHV replication [21,30]. This reflects the importance of the nsp10-nsp14 interaction surface in coronaviruses. Our results indicate that the same is valid for SARS-CoV-2, since nsp14 only shows a weak ExoN activity in the absence of nsp10, which is strongly enhanced upon interaction with nsp10 (also observed in [24]). We have further established that the concentration ratio for the nsp10/nsp14 complex of SARS-CoV-2 is 4 : 1, as this yielded maximal ExoN activity. The same ratio was observed for SARS-CoV [16].

Although the 3D structure of the SARS-CoV-2 nsp14-nsp10 complex is not yet solved, our work gave the first insights into important SARS-CoV-2 nsp10 residues directly involved in the interaction with nsp14. This is here demonstrated by the SPR data, as inferred by the homology model done on the basis of the SARS-CoV experimentally determined structure, and the high sequence identity between the proteins

from the two viruses. We demonstrate that mutations in the nsp10 F19, G69, S72, H80, and Y96 amino acid residues have deleterious consequences for the nsp14 ExoN activity *in vitro*, which could be rationalized by the structural effects that these mutations have in the formation of the nsp10-nsp14 heterodimer. Therefore, we infer that a stable interaction between these two proteins is strictly required for the correct functioning of nsp14 ExoN activity of SARS-CoV-2. Nsp10 mutations that disrupted the nsp10-nsp14 interaction were lethal for MHV and SARS-CoV, but the inactivation of the ExoN domain was not. However, this domain was found to be essential for the viability of SARS-CoV-2 (and also MERS) [15,21,30,35,36]. Thus, the nsp14 ExoN activity might have a predominant role on SARS-CoV-2 life cycle. The role of nsp10 is reinforced by its pleiotropic function during viral replication. Additionally to nsp14, nsp10 is also responsible for stimulating the nsp16 2'-O-MTase activity [20]. Nsp14 and nsp16 share a common interaction surface with nsp10. Some residues here identified as crucial for SARS-CoV-2 ExoN activation have already been recognized as essential for nsp16 2'-O-MTase activity [16,21,37]. Y96 targets both the nsp10-nsp14 and nsp10-nsp16 interactions in SARS-CoV [21]. The same seems to be valid for SARS-CoV-2 based in our results *in vitro* and on the crystal structure of the nsp10-nsp16 complex recently solved [38]. An alanine substitution in the residue S72 of nsp10, which has also been reported to be involved in SARS-CoV nsp10-nsp16 and nsp10-nsp14 interactions [21], resulted in a total loss of SARS-CoV-2 nsp10 ability to stimulate the exoribonucleolytic activity of nsp14. This mutant even seems to compromise the nsp14 basal activity, usually observed in the absence of nsp10. Therefore, inhibition of SARS-CoV-2 nsp10 could have an impact on several steps of viral RNA synthesis.

Our results highlighted nsp10 as a potential target for antiviral drug development. We propose some nsp10 residues that can be targeted to disrupt both the nsp14-nsp10 and nsp16-nsp10 complexes, leading simultaneously to inhibition of ExoN and 2'-O-MTase activities. Because this protein is highly conserved among CoVs, molecules developed to inhibit SARS-CoV-2 nsp10 interaction surface might be extended to other coronaviruses. To support this, Ogando and colleagues [15] reported the interchangeability of nsp10 between SARS-CoV and MERS. Indeed, the nsp10-derived peptide TP29, which was developed to target MHV nsp16 2'-O-MTase activity, successfully suppressed SARS-CoV replication in cell culture [39]. Importantly, nsp10 may be targeted by inhibitors with minimum cross-reactivity with human proteins, since

no structures with a fold similar to nsp10 were found in prokaryotes or eukaryotes [29].

We have also looked into the role of conserved DEDD catalytic residues for the ExoN activity of SARS-CoV-2 nsp14. Our results revealed that both motif I D90 and E92 amino acids are strictly required for the RNase activity of this protein, whereas mutations on motif II D243 and motif III D273 do not play such an important role. Thus, we would expect that D90 and E92 residues may have a large impact on SARS-CoV-2 replication. All the nsp14 D90A/E92A, D243A, and 273A substitutions that impaired SARS-CoV ExoN activity *in vitro* also displayed drastic effects *in vivo*. Less accumulation of viral RNA, defects in the synthesis of subgenomic RNAs, and a failure to recover infectious viral progeny were observed in HCoV 229E [23]. The same mutations abrogated detectable RNA synthesis and gave rise to nonviable MERS-CoV [15].

The most explored role of nsp14 ExoN so far is the repairing of mismatches that may be introduced during CoVs RNA synthesis. This capability has also been proposed to be responsible for the excision of nucleoside analogs that are incorporated into RNA, and lead to premature termination of viral RNA replication and survival [35,36,40,41]. Thus, the inhibition of nsp14 ExoN proofreading may potentiate the effect of nucleoside-based inhibitors, such as Remdesivir and Favipiravir [42,43]. It was previously seen that SARS-CoV and MHV mutants lacking nsp14 ExoN activity exhibited increased susceptibility to nucleoside inhibitors [21,35,36,40,41]. In particular, an MHV deficient in ExoN proofreading was significantly more sensitive to Remdesivir [42]. For these reasons, the combination of nucleoside analogs with nsp14 inhibitors may be more effective. As such, our biochemical results may be very important for the design of new molecules to inhibit the ExoN activity from SARS-CoV-2, which should be targeting the two important residues for catalysis, D90 and E92. These indications, together with the lack of sequence homology with the human proteome [44], make nsp14 an excellent druggable protein.

Pathogenic viruses that replicate in the cytoplasm have evolved mechanisms to facilitate infection of mammalian cells. These include the generation of cap structures on their RNA through methyltransferases (MTases) [45]. In this study, we have demonstrated for the first time the nsp14 N7-MTase activity of SARS-CoV-2. This activity is a key factor for equipping viral mRNAs with a functional 5'-terminal cap structure in order to be recognized by the cellular translation machinery. Unmethylated capped RNAs can induce

antiviral innate immune responses [46,47]. Here, we have reported that the nsp14 D331A substitution affects nsp14 MTase activity, which lost the capacity to methylate a capped RNA transcript to generate cap-0 ⁷MeGpppA-RNAs. This makes this residue also of special interest as a target of putative drugs.

Besides viral life cycle, nsp14 can also influence the immune response of the host cells. During the replication process of CoVs, the generated dsRNA intermediates are known to activate the type I interferon (IFN-I) response [48]. Nsp14 was indeed identified as one of the most potent interferon antagonists from SARS-CoV-2 [49]. In the present work, our results revealed the ability of nsp14 ExoN to cleave dsRNA. Thus, this protein may be involved in the degradation of viral dsRNA replication intermediates, hindering the activation of the host innate immune response. This hypothesis was already pointed for SARS-CoV and MERS-CoV [15,16].

As reported for other CoVs, our results also confirm that the 3'-5' exoribonucleolytic activity of nsp14 is dependent on metal ions, preferentially Mg²⁺ over Mn²⁺, Co²⁺, and Zn²⁺ promote residual activity, whereas Ca²⁺, Ni²⁺, and Cu²⁺ did not support catalysis. Zn²⁺ plays a crucial role in the stabilization of the nsp10 and nsp14 structures [17,29]. This importance was demonstrated in other studies by the observed aggregation or completely loss of function when a chelating agent was added to the assay buffer [16]. These conclusions are reinforced by the presence of 2 and 3 zinc fingers in nsp10 and nsp14, respectively. As is shown in Fig. 3B, at least one zinc finger of each of the two proteins may directly interact with and stabilize loop regions that are part of their interface of interaction. Moreover, nsp14 tested alone produced similar results to the reconstituted complex when using different divalent ions. Taking this into consideration, the effects observed on the ExoN activity are due to ion replacement in the activity site and not due to the interference on the complex formation caused by metal ion replacement in zinc fingers. It is tempting to speculate on divalent metals availability as major environmental determinants of the RNase activity of nsp14 *in vivo*. In this regard, alteration of ion homeostasis in favor of infection has been already demonstrated in several viral systems, including in SARS-CoV and MERS [50]. Even trace metals such as zinc and copper are known to influence the course and the outcome of a variety of viral infections [51].

More experimentation and structure information is nonetheless required to fully understand the precise functional and structural role of individual residues in SARS-CoV-2 nsp10 and nsp14 proteins. The

determination of the 3D structure of the nsp10/nsp14 complex will be also helpful to increase our knowledge about the synergies between these proteins and to validate our findings. Also, the effect of the nsp14 and nsp10 mutations here described should be employed in a reverse genetic approach in SARS-CoV-2 to study viral replication and transcription.

It was already demonstrated that CoV ExoN activity of nsp14, which is stimulated by nsp10, constitutes a critical regulator of viral RNA synthesis and degradation. Our results pinpoint the residues that are crucial for the complex formation and ExoN activity, which may be very important to discover new inhibitors that may be used to treat COVID-19 and other diseases caused by other CoVs.

Materials and methods

Plasmid construction

Full-length nsp10 and nsp14 genes from SARS-CoV2 (UniProt ID [P0DTD1](#)) were optimized for *E. coli* expression and synthesized by GenScript (USA). The synthesized genes were subsequently cloned into the *NdeI*–*Bam*HI sites of commercial pET15b to generate pET15b_Nsp10 and pET15b_Nsp14, which express N-terminal His-tagged versions of nsp10 and nsp14.

The point mutations F19A, G69A, S72A, H80A, and Y96A were introduced into pET15b_nsp10 by overlapping PCR using the primers listed in Table [S1](#). The point mutations D90A, E92A, D243A, D273A, and D331A were introduced into pET15b_nsp14 also by overlapping PCR (Table [S2](#)). All the constructions were verified by sequencing at StabVida (Portugal).

Protein expression and purification

Plasmids expressing nsp10 WT and point mutations were transformed into BL21 (DE3) cells, while plasmids expressing nsp14 WT and point mutations were transformed into Rosetta cells for the expression of the recombinant proteins. Cells were grown in LB medium supplemented with 150 $\mu\text{g}\cdot\text{mL}^{-1}$ ampicillin (nsp10 variants) or TB medium supplemented with 150 $\mu\text{g}\cdot\text{mL}^{-1}$ ampicillin and 50 $\mu\text{g}\cdot\text{mL}^{-1}$ chloramphenicol (nsp14 variants) at 30 °C to an OD_{600} of 0.5. At this point, protein expression was induced by addition of 0.5 mM IPTG and bacteria were grown for further 16 h. Cells were pelleted by centrifugation and stored at –80 °C. To copurify nsp10 with nsp14, cultures overexpressing each protein separately were pelleted together. The culture pellets were resuspended in 10 mL of Buffer A (40 mM Tris/HCl pH 8, 150 mM NaCl, 10 mM imidazole). Cell suspensions were lysed using the FastPrep-24 (MP Biomedical, Irvine, CA, USA) at 6.5 $\text{m}\cdot\text{s}^{-1}$ for 60 s in the presence of

0.5 mM PMSF. The crude extract was treated with Benzonase (Sigma, St. Louis, MI, USA) to degrade the nucleic acids and clarified by a 30 min of centrifugation at 10 000 *g*. Purification was performed in an ÄKTA FPLC™ system (Cytiva, Marlborough, MA, USA). The cleared lysate was subjected to a histidine affinity chromatography in a HisTrap HP column (Cytiva) equilibrated in Buffer A. Proteins were eluted by a continuous imidazole gradient up to 500 mM in Buffer A. The fractions containing the purified protein were pooled together and concentrated by centrifugation at 4 °C with Amicon Ultra Centrifugal Filter Devices of 10 000 MWCO (Millipore, Burlington, MA, USA) and buffer exchanged to Buffer B (20 mM Tris/HCl pH 8, 150 mM NaCl). Afterward, the proteins were subjected to a size-exclusion chromatography using a Superdex 200 Increase column (Cytiva) with a flow rate of 0.5 $\text{mL}\cdot\text{min}^{-1}$ using buffer B. The samples collected were analyzed in a 15% SDS/PAGE followed by BlueSafe staining (NZYTech, Portugal). Samples with the highest purity were pooled together and concentrated by centrifugation at 4 °C with Amicon Ultra Centrifugal Filter Devices of 10 000 MWCO (Millipore). All protein versions were purified at least twice to ensure reproducibility of the results. Proteins were quantified using the Bradford Method, and 50% (v/v) glycerol was added to the final fractions prior storage at –20 °C.

RNase activity assays

A synthetic 22-mer oligoribonucleotide (H4 5'-UGACGGCCCCGAAAACCGGGCC-3') (StabVida, Portugal) was used as a substrate in the activity assays. The RNA was labeled at its 5' end with [^{32}P]- γ -ATP and T4 Polynucleotide Kinase (Ambion) in a standard reaction. MicroSpin G-50 columns (Cytiva) were used to remove excess [^{32}P]- γ -ATP. In order to fold its 3'-end into a duplex structure, the RNA was resuspended in 10 mM of Tris/HCl pH 8.0 and incubated 10 min at 80 °C followed by 45 min at 37 °C.

The activity assays were performed in a final volume of 12 μL containing the activity buffer – 50 mM HEPES pH 7.4, 1 mM DTT, and 5 mM of either MgCl_2 , MnCl_2 , CaCl_2 , NiCl_2 , ZnCl_2 , CoCl_2 , or CuCl_2 —and the proteins nsp14 and nsp10 (protein concentrations are indicated in the figure legends). The reactions were started by the addition of 50 nM of the RNA substrate and further incubated at 37 °C. Aliquots of 4 μL were withdrawn at the time points indicated in the respective figures, and the reactions were stopped by the addition of formamide-containing dye supplemented with 10 mM EDTA. A control reaction containing only the RNA substrate and the activity buffer (without the enzyme) was incubated in the same conditions during the full time of the assay. Reaction products were resolved in a 20% denaturant polyacrylamide gel (7 M urea). Signals were visualized by PhosphorImaging (TLA-

5100 Series, Fuji). All the experiments were performed at least in triplicate. Disappearance of substrate along time was quantified using the ImageQuant (Cytiva).

Surface plasmon resonance

Surface plasmon resonance (SPR) was performed by using a CM5 sensor chip (Cytiva) and a Biacore 2000 system (Cytiva). Purified nsp14 was immobilized in flow cell 2 of the CM5 sensor chip by the amine coupling procedure. The surface was activated with a 1 : 1 mixture of 1-ethyl-3-(3-dimethylaminopropyl) carbodiimide (EDC) and N-hydroxysuccinimide (NHS), injected during 5 min at a flow rate of 10 $\mu\text{L}\cdot\text{min}^{-1}$. Then, 20 $\mu\text{g}\cdot\text{mL}^{-1}$ of nsp14 was injected during 10 min at the same flow rate. After the injection of the ligand, ethanolamine was injected over the surface to deactivate it. The immobilization of the protein originated a response of 400 RU. On flow cell 1 (used as a control), BSA protein was immobilized using the same method. Biosensor assays were run at 15 °C in a buffer with 25 mM HEPES/HCl pH 7.4, 0.5 mM DTT, and 2.5 mM of MgCl_2 . Serial dilutions of purified Nsp10 WT and mutant proteins were injected overflow cells 2–1 for 3 min at concentrations of 50, 100, 175, 250, and 500 nM using a flow rate of 20 $\text{mL}\cdot\text{min}^{-1}$. The dissociation was allowed to occur during 5 min in the running buffer. All experiments included triple injections of each protein concentration to determine the reproducibility of the signal. Bound proteins were removed after each cycle with a 30-s wash with 2 M NaCl. After each cycle, the signal was stabilized during 1 min before the next protein injection. Data from flow cell 1 was used to correct refractive index changes and nonspecific binding.

Preparation of the capped RNA substrate

A 30-mer RNA substrate was first synthesized using a synthetic DNA template and a promoter oligonucleotide obtained by commercial source (StabVida) for *in vitro* transcription, using the method described by Ref. [52]. Briefly, the DNA synthetic template (0.5 μM) and the T7 promoter oligonucleotide (0.6 μM) were annealed in 10 mM of Tris/HCl pH 8.0 by heating for 5 min at 70 °C, following by incubation for 30 min, at 37 °C. *In vitro* transcription was carried out using 'NZY T7 High Yield RNA Synthesis kit' (NZYtech) following manufacturer instructions. To remove the DNA template, 1 U of DNase (Invitrogen) was then added to the reaction and incubated 15 min at 37 °C. Non-incorporated ribonucleotides were removed with Microspin G-50 Columns (Cytiva).

For the insertion of a ^{32}P -labeled cap structure (G*ppp-RNA) in the 5' end of 30 mer RNA substrate, we used the vaccinia virus capping enzyme following the manufacturer's protocol (New England Biolabs), except that the methyl

donor SAM was absent and 0.05 units of inorganic pyrophosphatase (New England Biolabs) were added to improve the efficiency of the reaction. A parallel reaction was prepared following the manufacturer's protocol (New England Biolabs) and using 2 mM SAM to obtain $\text{m}^7\text{G}^*\text{ppp-RNA}$. Nonincorporated radioisotope was removed using Microspin G-50 Columns (Cytiva), and the labeled substrate was then purified by phenol–chloroform extraction and ethanol precipitation. A small fraction of $\text{m}^7\text{G}^*\text{ppp-RNA}$ and of G*ppp-RNA were digested with 5 μg nuclease P1 (Sigma) in 50 mM NaOAc pH5.2 buffer to originate the $\text{m}^7\text{G}^*\text{ppp}$ and G*pppG markers in the TLC run.

Mtase activity assays

To test MTase activity of nsp14 WT or mutant versions, a reaction mix containing the purified recombinant protein (~1 μg), approximately 2 μg of ^{32}P -labeled 30-mer G*ppp-RNA substrate, 0.1 mM of SAM, an RNase inhibitor, and 2 mM DTT in a total volume of 20 μL , was prepared in the reaction buffer 50 mM HEPES pH 7.4, 1 mM DTT, 5 mM MgCl_2 , and 50 mM KCl, and incubated at 37 °C for 30 min. The same reaction without nsp14 treatment was performed as control. To liberate the cap structures, both RNAs (with and without nsp14 treatment) were digested with 1.25 units of nuclease P1 (Sigma) in 50 mM NaOAc pH5.2 buffer for 30 min at 37 °C, followed by the inactivation of the enzyme (75 °C for 10 min). The MTase activity of nsp14 WT (~0.05 μg) in the presence of nsp10 (1 : 2 and 1 : 4 ratios) was also performed using the same procedure. A TLC analysis was performed to separate G*pppG from capped $\text{m}^7\text{G}^*\text{pppG}$. For this, polyethylenimine cellulose-F plates (Merck, Burlington, MA, USA) were previously pre-run with water, air-dried, and then spotted with 2–3 μL of the P1 digestion reaction (1 μL spotted at each time, and let dry) and developed in 0.4 M ammonium sulfate. The $\text{m}^7\text{G}^*\text{pppG}$ and G*pppG markers (see above) were run in parallel. The chromatograms were then scanned with a PhosphorImager (TLA-5100 Series, Fuji) to evaluate the extent of ^{32}P -labeled capping. All the experiments were performed at least in triplicate.

Protein modeling

Modeling of the SARS-CoV-2 nsp10/nsp14 complex was done with the program MODELLER version 9.23 [53]. The crystal structure of the corresponding complex on SARS-CoV (PDB ID 5C8S) was used as the template for the homology modeling [17]. The catalytic and metal-binding amino acids were kept fixed during the model refinement stages. Twelve independent models were generated and ranked using the normalized DOPE score [54]. Subsequent analyses were carried on the model with the lowest score.

The final model was further used as the template for modeling the structures of the mutant proteins. Only the substituted residue and its neighboring residues (within 6 Å) were refined during the modeling process.

Acknowledgements

We are grateful to the distinguished and experienced virologists Miguel Fevereiro and Margarida Henriques (INIAV, Lisbon, Portugal) for the valuable discussions regarding physiology of SARS-CoV-2. We also thank Teresa Batista da Silva for technical support and Miguel Luís for helping with the graphical abstract. This work was funded by national funds through FCT—Fundação para a Ciência e a Tecnologia, I. P., Project MOSTMICRO-ITQB with refs UIDB/04612/2020 and UIDP/04612/2020. Project PTDC/BIA-BQM/28479/2017 to R.G.M, and project PTDC/CCI-BIO/28200/2017 to D.L. R.G.M and was also financed by an FCT contract (ref. CEECIND/02065/2017). SCV was financed by FCT program IF (ref. IF/00217/2015). M.S., S.D., and D.L. were financed by an FCT contract according to DL57/2016, [SFRH/BPD/109464/2015], [SFRH/BPD/84080/2012], and [SFRH/BPD/92537/2013], respectively. V.G.C. and C.B. have a fellowship and a contract, respectively, under the project PTDC/BIA-BQM/28479/2017. C.S.S. was financed by a fellowship under the project ShikiFactory100, grant agreement number 814408 from the European Union's Horizon 2020 research and innovation program.

Conflicts of interest

The authors declare no conflict of interest.

Author contributions

MS and RGM designed the experiments and coordinated the work; MS, CB, VGC, CSS, SCV, SD, DL, and RGM performed the experimental work. CMS and CMA promoted critical thinking. All authors contributed to the discussion of the work, wrote, and approved the final manuscript.

References

- Hu B, Guo H, Zhou P & Shi ZL (2020) Characteristics of SARS-CoV-2 and COVID-19. *Nature reviews. Microbiology* **19**, 141–154.
- Fung TS & Liu DX (2019) Human coronavirus: host-pathogen interaction. *Annu Rev Microbiol* **73**, 529–557.
- Arraiano CM, Andrade JM, Domingues S, Guinote IB, Malecki M, Matos RG, Moreira RN, Pobre V, Reis FP, Saramago M *et al.* (2010) The critical role of RNA processing and degradation in the control of gene expression. *FEMS Microbiol Rev* **34**, 883–923.
- Matos RG, Barria C, Moreira RN, Barahona S, Domingues S & Arraiano CM (2014) The importance of proteins of the RNase II/RNB-family in pathogenic bacteria. *Front Cell Infect Microbiol* **4**, 68.
- Saramago M, Barria C, Arraiano CM & Domingues S (2015) Ribonucleases, antisense RNAs and the control of bacterial plasmids. *Plasmid* **78**, 26–36.
- Saramago M, Barria C, Dos Santos RF, Silva IJ, Pobre V, Domingues S, Andrade JM, Viegas SC & Arraiano CM (2014) The role of RNases in the regulation of small RNAs. *Curr Opin Microbiol* **18**, 105–115.
- Saramago M, da Costa PJ, Viegas SC & Arraiano CM (2019) The implication of mRNA degradation disorders on human disease: focus on DIS3 and DIS3-like enzymes. *Adv Exp Med Biol* **1157**, 85–98.
- Ogando NS, Ferron F, Decroly E, Canard B, Posthuma CC & Snijder EJ (2019) The curious case of the nidovirus exoribonuclease: its role in RNA synthesis and replication fidelity. *Front Microbiol* **10**, 1813.
- Zuo Y & Deutscher MP (2001) Exoribonuclease superfamilies: structural analysis and phylogenetic distribution. *Nucleic Acids Res* **29**, 1017–1026.
- Beese LS & Steitz TA (1991) Structural basis for the 3'-5' exonuclease activity of Escherichia coli DNA polymerase I: a two metal ion mechanism. *The EMBO journal* **10**, 25–33.
- Deutscher MP & Marlor CW (1985) Purification and characterization of Escherichia coli RNase T. *The Journal of biological chemistry* **260**, 7067–7071.
- Steitz TA & Steitz JA (1993) A general two-metal-ion mechanism for catalytic RNA. *Proc Natl Acad Sci USA* **90**, 6498–6502.
- Snijder EJ, Bredenbeek PJ, Dobbe JC, Thiel V, Ziebuhr J, Poon LL, Guan Y, Rozanov M, Spaan WJ & Gorbalenya AE (2003) Unique and conserved features of genome and proteome of SARS-coronavirus, an early split-off from the coronavirus group 2 lineage. *J Mol Biol* **331**, 991–1004.
- Zhou P, Yang XL, Wang XG, Hu B, Zhang L, Zhang W, Si HR, Zhu Y, Li B, Huang CL *et al.* (2020) A pneumonia outbreak associated with a new coronavirus of probable bat origin. *Nature* **579**, 270–273.
- Ogando NS, Zevenhoven-Dobbe JC, van der Meer Y, Bredenbeek PJ, Posthuma CC & Snijder EJ (2020) The enzymatic activity of the nsp14 exoribonuclease is critical for replication of MERS-CoV and SARS-CoV-2. *J Virol* **94**.
- Bouvet M, Imbert I, Subissi L, Gluais L, Canard B & Decroly E (2012) RNA 3'-end mismatch excision by the severe acute respiratory syndrome coronavirus nonstructural protein nsp10/nsp14 exoribonuclease complex. *Proc Natl Acad Sci USA* **109**, 9372–9377.

- 17 Ma Y, Wu L, Shaw N, Gao Y, Wang J, Sun Y, Lou Z, Yan L, Zhang R & Rao Z (2015) Structural basis and functional analysis of the SARS coronavirus nsp14-nsp10 complex. *Proc Natl Acad Sci USA* **112**, 9436–9441.
- 18 Chen Y, Cai H, Pan J, Xiang N, Tien P, Ahola T & Guo D (2009) Functional screen reveals SARS coronavirus nonstructural protein nsp14 as a novel cap N7 methyltransferase. *Proc Natl Acad Sci USA* **106**, 3484–3489.
- 19 Jin X, Chen Y, Sun Y, Zeng C, Wang Y, Tao J, Wu A, Yu X, Zhang Z, Tian J *et al.* (2013) Characterization of the guanine-N7 methyltransferase activity of coronavirus nsp14 on nucleotide GTP. *Virus Res* **176**, 45–52.
- 20 Chen Y, Su C, Ke M, Jin X, Xu L, Zhang Z, Wu A, Sun Y, Yang Z, Tien P *et al.* (2011) Biochemical and structural insights into the mechanisms of SARS coronavirus RNA ribose 2'-O-methylation by nsp16/nsp10 protein complex. *PLoS Pathog* **7**, e1002294.
- 21 Bouvet M, Lugari A, Posthuma CC, Zevenhoven JC, Bernard S, Betzi S, Imbert I, Canard B, Guillemot JC, Lecine P *et al.* (2014) Coronavirus Nsp10, a critical co-factor for activation of multiple replicative enzymes. *The Journal of biological chemistry* **289**, 25783–25796.
- 22 Su D, Lou Z, Sun F, Zhai Y, Yang H, Zhang R, Joachimiak A, Zhang XC, Bartlam M & Rao Z (2006) Dodecamer structure of severe acute respiratory syndrome coronavirus nonstructural protein nsp10. *J Virol* **80**, 7902–7908.
- 23 Minskaia E, Hertzog T, Gorbalenya AE, Campanacci V, Cambillau C, Canard B & Ziebuhr J (2006) Discovery of an RNA virus 3'->5' exoribonuclease that is critically involved in coronavirus RNA synthesis. *Proc Natl Acad Sci USA* **103**, 5108–5113.
- 24 Baddock HT, Brolih S, Yosaatmadja Y, Ratnaweera M, Bielinski M, Swift LP, Cruz-Migoni A, Morris GM, Schofield CJ, Gileadi O *et al.* (2020) Characterisation of the SARS-CoV-2 ExoN (nsp14ExoN-nsp10) complex: implications for its role in viral genome stability and inhibitor identification. *bioRxiv* [PREPRINT].
- 25 Chen P, Jiang M, Hu T, Liu Q, Chen XS & Guo D (2007) Biochemical characterization of exoribonuclease encoded by SARS coronavirus. *J Biochem Mol Biol* **40**, 649–655.
- 26 Saramago M, Peregrina A, Robledo M, Matos RG, Hilker R, Serrania J, Becker A, Arraiano CM & Jimenez-Zurdo JI (2017) Sinorhizobium meliloti YbeY is an endoribonuclease with unprecedented catalytic features, acting as silencing enzyme in riboregulation. *Nucleic Acids Res* **45**, 1371–1391.
- 27 Saramago M, Robledo M, Matos RG, Jimenez-Zurdo JI & Arraiano CM (2018) Sinorhizobium meliloti RNase III: catalytic features and impact on symbiosis. *Frontiers in genetics* **9**, 350.
- 28 Derbyshire V, Freemont PS, Sanderson MR, Beese L, Friedman JM, Joyce CM & Steitz TA (1988) Genetic and crystallographic studies of the 3',5'-exonucleolytic site of DNA polymerase I. *Science* **240**, 199–201.
- 29 Rogstam A, Nyblom M, Christensen S, Sele C, Talibov VO, Lindvall T, Rasmussen AA, Andre I, Fisher Z, Knecht W *et al.* (2020) Crystal structure of non-structural protein 10 from severe acute respiratory syndrome coronavirus-2. *Int J Mol Sci* **21**, 7375.
- 30 Donaldson EF, Sims AC, Graham RL, Denison MR & Baric RS (2007) Murine hepatitis virus replicase protein nsp10 is a critical regulator of viral RNA synthesis. *J Virol* **81**, 6356–6368.
- 31 Lugari A, Betzi S, Decroly E, Bonnaud E, Hermant A, Guillemot JC, Debarnot C, Borg JP, Bouvet M, Canard B *et al.* (2010) Molecular mapping of the RNA Cap 2'-O-methyltransferase activation interface between severe acute respiratory syndrome coronavirus nsp10 and nsp16. *The Journal of biological chemistry* **285**, 33230–33241.
- 32 Cunningham BC & Wells JA (1989) High-resolution epitope mapping of hGH-receptor interactions by alanine-scanning mutagenesis. *Science* **244**, 1081–1085.
- 33 Chen Y, Tao J, Sun Y, Wu A, Su C, Gao G, Cai H, Qiu S, Wu Y, Ahola T *et al.* (2013) Structure-function analysis of severe acute respiratory syndrome coronavirus RNA cap guanine-N7-methyltransferase. *J Virol* **87**, 6296–6305.
- 34 Bouvet M, Debarnot C, Imbert I, Selisko B, Snijder EJ, Canard B & Decroly E (2010) In vitro reconstitution of SARS-coronavirus mRNA cap methylation. *PLoS Pathog* **6**, e1000863.
- 35 Eckerle LD, Becker MM, Halpin RA, Li K, Venter E, Lu X, Scherbakova S, Graham RL, Baric RS, Stockwell TB *et al.* (2010) Infidelity of SARS-CoV Nsp14-exonuclease mutant virus replication is revealed by complete genome sequencing. *PLoS Pathog* **6**, e1000896.
- 36 Eckerle LD, Lu X, Sperry SM, Choi L & Denison MR (2007) High fidelity of murine hepatitis virus replication is decreased in nsp14 exoribonuclease mutants. *J Virol* **81**, 12135–12144.
- 37 Ferron F, Subissi L, Silveira De Moraes AT, Le NTT, Sevajol M, Gluais L, Decroly E, Vonrhein C, Bricogne G, Canard B *et al.* (2018) Structural and molecular basis of mismatch correction and ribavirin excision from coronavirus RNA. *Proc Natl Acad Sci USA* **115**, E162–E171.
- 38 Lin S, Chen H, Ye F, Chen Z, Yang F, Zheng Y, Cao Y, Qiao J, Yang S & Lu G (2020) Crystal structure of SARS-CoV-2 nsp10/nsp16 2'-O-methylase and its implication on antiviral drug design. *Signal Transduct Target Therapy* **5**, 131.
- 39 Wang Y, Sun Y, Wu A, Xu S, Pan R, Zeng C, Jin X, Ge X, Shi Z, Ahola T *et al.* (2015) Coronavirus nsp10/

- nsp16 methyltransferase can be targeted by nsp10-derived peptide in vitro and in vivo to reduce replication and pathogenesis. *J Virol* **89**, 8416–8427.
- 40 Graepel KW, Lu X, Case JB, Sexton NR, Smith EC & Denison MR (2017) Proofreading-deficient coronaviruses adapt for increased fitness over long-term passage without reversion of exoribonuclease-inactivating mutations. *MBio* **8**, e01503–17.
- 41 Smith EC, Blanc H, Surdel MC, Vignuzzi M & Denison MR (2013) Coronaviruses lacking exoribonuclease activity are susceptible to lethal mutagenesis: evidence for proofreading and potential therapeutics. *PLoS Pathog* **9**, e1003565.
- 42 Agostini ML, Andres EL, Sims AC, Graham RL, Sheahan TP, Lu X, Smith EC, Case JB, Feng JY, Jordan R, Ray AS. Coronavirus susceptibility to the antiviral remdesivir (GS-5734) is mediated by the viral polymerase and the proofreading exoribonuclease. *mBio* **9**, e00221–18.
- 43 Shannon A, Le NT, Selisko B, Eydoux C, Alvarez K, Guillemot JC, Decroly E, Peersen O, Ferron F & Canard B (2020) Remdesivir and SARS-CoV-2: Structural requirements at both nsp12 RdRp and nsp14 exonuclease active-sites. *Antiviral Res* **178**, 104793.
- 44 Gurung AB (2020) In silico structure modelling of SARS-CoV-2 Nsp13 helicase and Nsp14 and repurposing of FDA approved antiviral drugs as dual inhibitors. *Gene reports* **21**, 100860.
- 45 Hyde JL & Diamond MS (2015) Innate immune restriction and antagonism of viral RNA lacking 2-O methylation. *Virology* **479–480**, 66–74.
- 46 Daffis S, Szretter KJ, Schriewer J, Li J, Youn S, Errett J, Lin TY, Schneller S, Zust R, Dong H *et al.* (2010) 2'-O methylation of the viral mRNA cap evades host restriction by IFIT family members. *Nature* **468**, 452–456.
- 47 Ramanathan A, Robb GB & Chan SH (2016) mRNA capping: biological functions and applications. *Nucleic Acids Res* **44**, 7511–7526.
- 48 Rehwinkel J & Gack MU (2020) RIG-I-like receptors: their regulation and roles in RNA sensing. *Nat Rev Immunol* **20**, 537–551.
- 49 Yuen CK, Lam JY, Wong WM, Mak LF, Wang X, Chu H, Cai JP, Jin DY, To KK, Chan JF *et al.* (2020) SARS-CoV-2 nsp13, nsp14, nsp15 and orf6 function as potent interferon antagonists. *Emerg Microbes Infect* **9**, 1418–1428.
- 50 Nieto-Torres JL, Verdia-Baguena C, Jimenez-Guardeno JM, Regla-Nava JA, Castano-Rodriguez C, Fernandez-Delgado R, Torres J, Aguilera VM & Enjuanes L (2015) Severe acute respiratory syndrome coronavirus E protein transports calcium ions and activates the NLRP3 inflammasome. *Virology* **485**, 330–339.
- 51 Chaturvedi UC & Shrivastava R (2005) Interaction of viral proteins with metal ions: role in maintaining the structure and functions of viruses. *FEMS Immunol Med Microbiol* **43**, 105–114.
- 52 Milligan JF, Groebe DR, Witherell GW & Uhlenbeck OC (1987) Oligoribonucleotide synthesis using T7 RNA polymerase and synthetic DNA templates. *Nucleic Acids Res* **15**, 8783–8798.
- 53 Sali A & Blundell TL (1993) Comparative protein modelling by satisfaction of spatial restraints. *J Mol Biol* **234**, 779–815.
- 54 Shen MY & Sali A (2006) Statistical potential for assessment and prediction of protein structures. *Protein Sci* **15**, 2507–2524.

Supporting information

Additional supporting information may be found online in the Supporting Information section at the end of the article.

Table S1. Primers used in this study; bases changes are underlined.

Table S2. Plasmids used in this study.